Effects of thermal instability on density limit disruption in J-TEXT
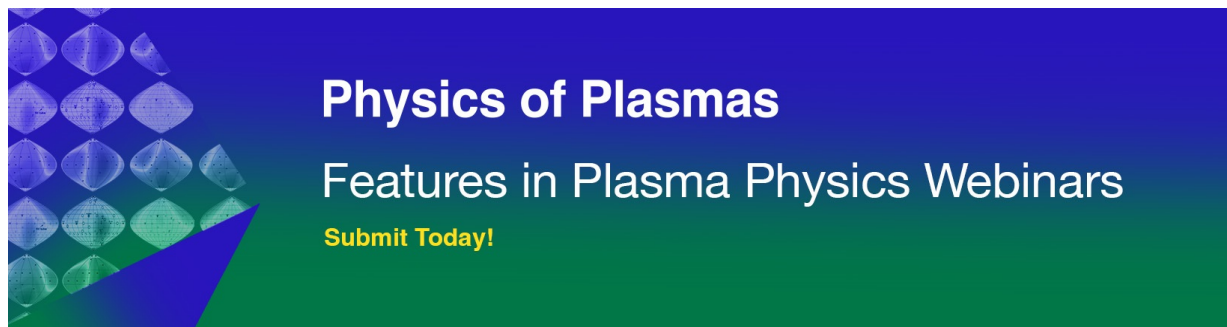
J. J. Yuan, Z. H. Jiang, Y. Liang, et al.

View Online

Export Citation

CrossMark

Physics of Plasmas

Features in Plasma Physics Webinars

Submit Today!

AIP Publishing

29, 123904

Effects of thermal instability on density limit disruption in J-TEXT

View Online   Export Citation   CrossMark

J. J. Yuan,[1,2] Z. H. Jiang,[1,a)] Y. Liang,[1,3,4] Z. X. Jiao,[1] Z. Li,[1] J. K. Hua,[1] L. Gao,[1] Z. Y. Chen,[1] Y. H. Ding,[1] and J-TEXT Team[b)]

AFFILIATIONS

[1] International Joint Research Laboratory of Magnetic Confinement Fusion and Plasma Physics, State Key Laboratory of Advanced Electromagnetic Engineering and Technology, School of Electrical and Electronic Engineering, Huazhong University of Science and Technology, Wuhan 430074, People's Republic of China
[2] China Electric Power Research Institute Co., Ltd., Wuhan 430074, China
[3] Institute of Plasma Physics, Chinese Academy of Sciences, Hefei 230031, People's Republic of China
[4] Forschungszentrum Jülich GmbH, Institut für Energie-und Klimaforschung-Plasmaphysik, Jülich 52425, Germany

[a)] Author to whom correspondence should be addressed: zhhjiang@hust.edu.cn
[b)] See the author list of Wang *et al.*, Nucl. Fusion **62**, 042016 (2022).

ABSTRACT

As an important precursor of density limit disruption, thermal instability under J-TEXT high-density discharges is studied in this paper. An extended MHD code called NIMROD [Sovinec *et al.*, J. Comput. Phys. **195**, 355 (2004)] is used to explore the intrinsic relationship between density limit disruption and thermal instability. The experimental and simulation results show that radiation from the boundary impurity can cause thermal instability and impurity radiation increases rapidly when the plasma temperature decreases to the nonlinear range of carbon cooling rates, which cools down the plasma and enhances impurity radiation. Further investigations show that the local reduction in thermal instability at the plasma edge shrinks the local current channel and increases the internal current density gradient, which triggers the 2/1 mode and destabilizes the 3/1 and other higher-order modes. Finally, a rapid increase in the MHD instability can cause density limit disruption.

Published under an exclusive license by AIP Publishing. https://doi.org/10.1063/5.0110818

I. INTRODUCTION

Realizing steady operation at high density is necessary to achieve high thermonuclear power of future tokamaks. However, this is impeded by the existence of a density limit.[1,2] Based on the results of the Murakami–Hugill density limit,[1–3] Greenwald defined a scaling law named the Greenwald density limit,[4] which is expressed as follows:

$$n_e^{GW}(10^{20}m^{-3}) = I_P(\text{MA})/(\pi a^2(m^2)), \qquad (1)$$

where I_p is the plasma current, a is the minor radius, and n_e^{GW} is the plasma density.

The ubiquitous limit on plasma density has been observed in different machines with various configurations.[5] According to the early theory of Wesson, density limit disruption is triggered by the appearance of $m/n = 2/1$ tearing mode,[6] where m denotes the poloidal mode number and n is the toroidal mode number. Based on this, many mechanisms have been developed to associate the density limit with
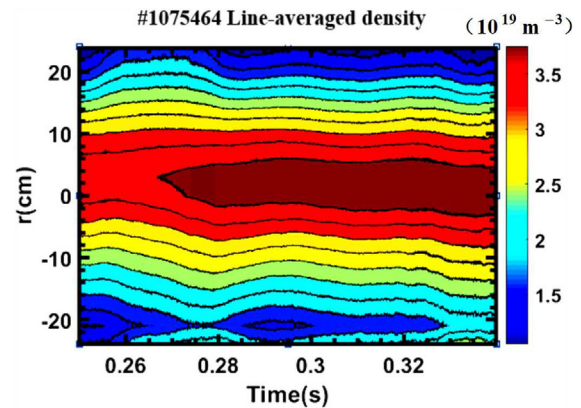
radiation.[7–11] A model of radiation-driven thermo-resistive islands, which can provide a possible explanation of the physical mechanism of the density limit, was proposed.[9–11] In the J-TEXT high-density discharges, multi-faceted asymmetric radiation from the edge (MARFE) appears before the 2/1 magnetic island arises.[12–14] Experimental observations have shown that thermal instability is the precursor of MARFE and density limit disruption and have expressed a direct relationship between thermal instability and density limit.[15,16] However, this problem has not been investigated systematically from the aspect of the appearance of thermal instability due to density limit disruption.

In general, the thermal instability is caused by the temperature dependence of radiative and atomic physics cooling mechanisms, which is due to the line radiation of light impurities in the tokamak boundary that decreases local temperature.[17–21] Therefore, thermal instability has been considered a vital cause of the formation of MARFE.[22–27] Accordingly, based on the linear stability analysis of the coupled energy and particle conservation equations, density, and
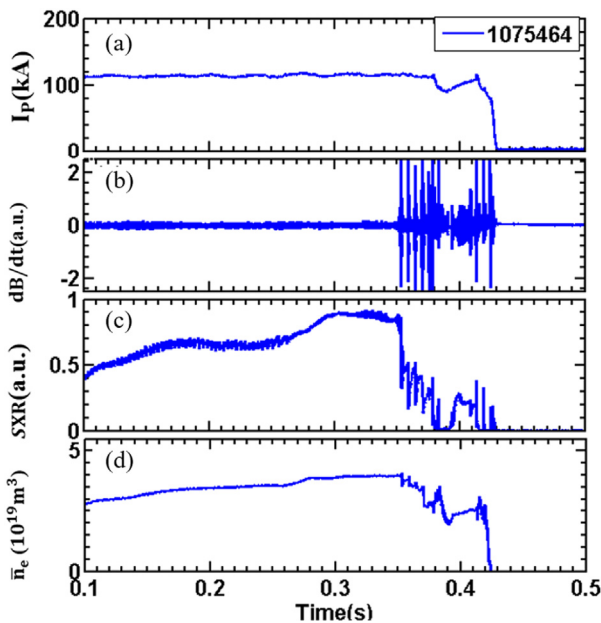
FIG. 1. Typical high-density limit discharge (No. 1 075 464). (a) Total plasma current; (b) Mirnov signal; (c) soft x-ray (SXR) signal; and (d) central line-averaged density.

FIG. 2. Time evolution of the radial distribution of line-averaged density.

temperature equations, Stacey analyzed the collapse of the temperature profile in detail and defined the density criterion of temperature and density profile collapse.[28] A fluid model with two-dimensional (2D) tokamak equilibria was applied to study the thermal instability of MARFE by Ploey.[29] In this study, a 2D linear stability analysis of thermal instability was presented, focusing on the parameters' variations at the initial moment of thermal instability. However, the aforementioned works did not comprehensively explore the effects of thermal instability on the plasma density and radiation heightening, but these effects can collapse the temperature profile of the plasma boundary region, shrink the current channel, trigger the MHD tearing mode, and finally lead to the density limit disruption. Therefore, this paper examines the effects of thermal instability on the density limit disruption through the J-TEXT experiments using a nonideal theoretical MHD model. In addition, three-dimensional (3D) nonlinear simulations are conducted to study thermal instability by the NIMROD code. The extensive simulation results show that thermal instability at the plasma boundary plays an important role in the growth of the 2/1 island. The increase in instability shrinks the plasma current channel, thus increasing the current density gradient at the 2/1 surface and finally leading to the density limit disruption.

In this paper, thermal instability is realized by artificially introducing impurities (carbon) in the killer pellet radiation (KPRAD) module of the NIMROD code. The rest of the paper is organized as follows. Section II presents the thermal instability results obtained in
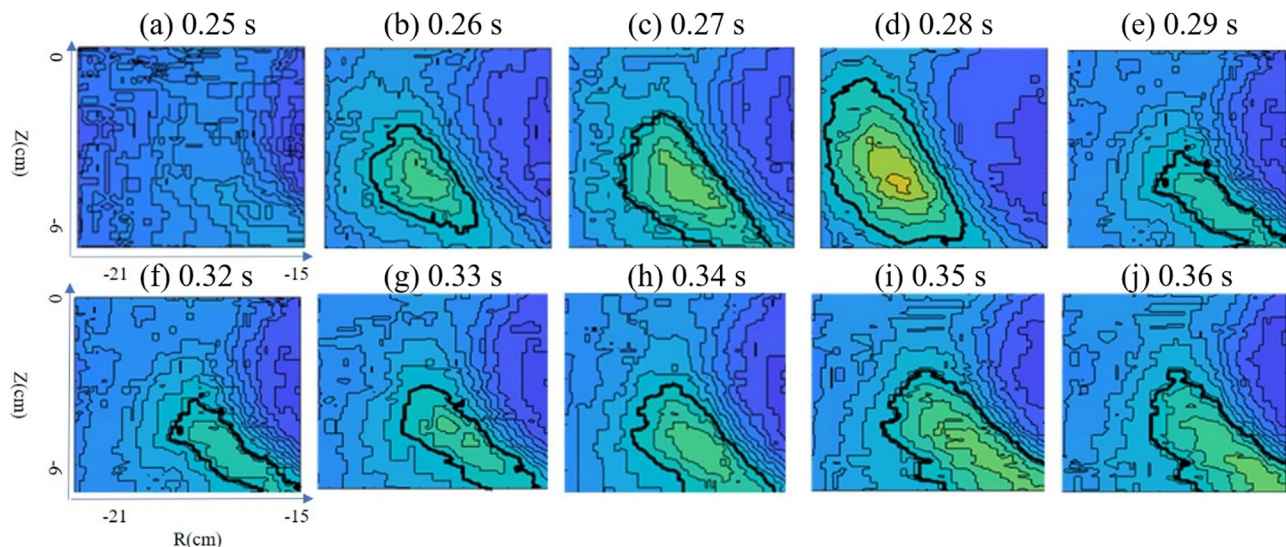
FIG. 3. CCD camera records of shot No. 1 075 464 on the J-TEXT.

the J-TEXT high-density experiment. Section III introduces the numerical model used in the simulations. Section IV presents the simulation results of the thermal instability evolution and analyzes the effects of thermal instability on the plasma density limit disruption. Section V discusses the simulation results and makes the corresponding conclusions.

II. RESULTS OF THERMAL INSTABILITY EVOLUTION IN J-TEXT HIGH-DENSITY EXPERIMENT

A. Experimental setup

The J-TEXT, which represents a medium-sized circular tokamak with a major radius of $R_0 = 1.05$ m and a minor radius of $a = 0.25$–0.29 m, was used in the experiment. In the J-TEXT, the first wall and the limiter were covered with carbon tiles. The discharges were performed in Ohmic heating, and the working gas was hydrogen. The J-TEXT was operated in a limiter configuration with a toroidal magnetic field of $B_t = 1.8$ T at the magnetic axis. The other basic plasma parameters were $I_p = 120$ kA and $a = 0.255$ m, and the edge safety factor was $q_a = 4.6$.

B. Experimental results

The experimental results of high-density discharges in the J-TEXT confirmed that thermal instability appeared as the plasma density approached the upper limit. The typical high-density disruption discharge on the J-TEXT is presented in Fig. 1, where the data obtained from shot No. 1 075 464 are presented. The discharge terminated at $t = 0.42$ s, and the maximum central line-averaged density was 4×10^{19} m^{-3} = $0.67 n_G$, where n_G denotes the Greenwald density limit. During the interval of 0.1 s $< t < 0.35$ s, the central line-averaged electron density increased, as shown in Fig. 1(d), and multistage collapse appeared at 0.35 s. Meanwhile, the multistage collapse of the soft x-ray (SXR) signal could be observed at 0.35 s
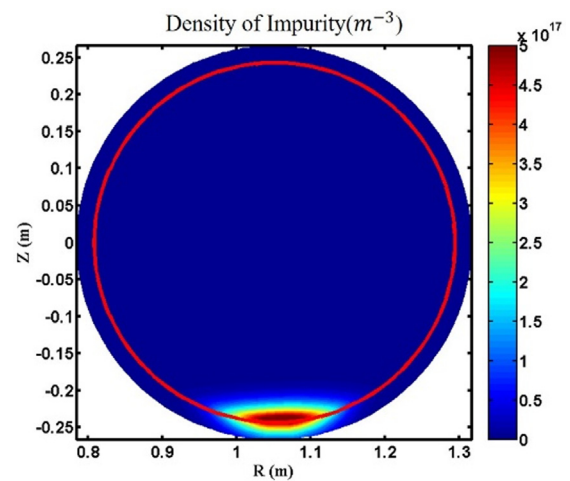

FIG. 4. Normalized poloidal distribution of carbon impurity; the blue circle represents vacuum and plasma regions.

accompanied by a burst of MHD activities, as shown in Figs. 1(b) and 1(c).

A detailed illustration of the radial distribution of line-averaged density can be found in Fig. 2, where it can be seen that an asymmetry of line-averaged density occurred between the very edge of the low-field side (LFS), whose minor radius was approximately 21 cm, and the high-field side (HFS), with $r = -21$ cm. Therefore, it could be concluded that electron density asymmetry occurred at the edge. In addition, a visible CCD camera recorded a bright blob evolution at the HFS edge, after which asymmetric plasma behaviors occurred, as shown in Fig. 3. In Fig. 2, it can be observed that a bright blob appeared at the plasma edge at $t = 0.26$ s, and the blob became brighter and moved into the plasma region at $t = 0.28$ s, and the asymmetry in line-averaged density was enhanced. The bright blob stayed inside the
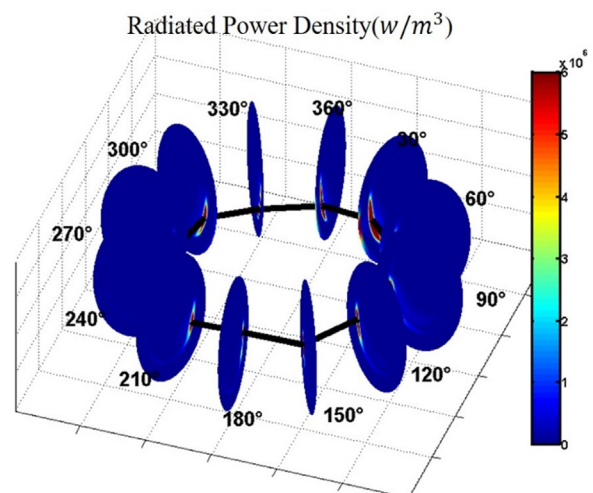
TABLE I. Main input parameters of the density limit simulation.

Parameter	Position	Value	Unit
Core resistivity (η)	Plasma core	2.8×10^{-8}	$\Omega\,m$
Core plasma density (n_e)	Plasma core	2×10^{19}	m^{-3}
Boundary plasma density (n_e)	Plasma edge	5×10^{18}	m^{-3}
Core plasma temperature (T_e)	Plasma core	750	eV
Particle diffusion coefficient (D)	Uniform	1	m^2/s
Core parallel thermal diffusion ($\chi_{//}$)	Plasma core	1×10^8	m^2/s
Boundary parallel thermal diffusion ($\chi_{//}$)	Plasma edge	1×10^5	m^2/s
Core perpendicular thermal diffusion ($\chi_{\perp}$)	Plasma core	0.1	m^2/s
Boundary perpendicular thermal diffusion ($\chi_{\perp}$)	Plasma edge	1	m^2/s
Plasma current (I_p)	/	120	kA
Toroidal magnetic (B_t)	/	1.8	T

FIG. 5. Toroidal distribution of radiation power density; contours denote the poloidal distribution of radiation at different toroidal locations, and the black line connects the positions of maximum radiation in each poloidal plane.

plasma edge region, and the discharge was terminated by a density limit disruption at $t = 0.42$ s.

The experimental results showed that the J-TEXT shot No. 1 075 464 had some of the basic characteristics of a high-density discharge. However, the conducted limited diagnostic measurements could not fully determine the physics mechanism of density limit disruption. Therefore, the MHD fluid model was used to study the effect of thermal instability on the density limit discharge through numerical simulations. Important experimental parameters were input into the NIMROD code, and the evolution of plasma parameters was used to explore the effects of thermal instability on the J-TEXT high-density discharge. Specific research results are presented in the Sec. III.

III. SIMULATION MODEL

The simulations were performed using the NIMROD code. The equations of temperature, number density, velocity, and magnetic field were solved by this code using a nonlinear single-fluid, resistive MHD model. In addition, the code was coupled with a simplified model for impurity radiation developed based on the KPRAD module. This combined model has been previously used in rapid shutdown experiments of impurity injection into tokamak plasmas for disruption mitigation in the DIII-D and J-TEXT.[30–37] The equations used in the simulations were as follows:

$$\rho \frac{d\boldsymbol{V}}{dt} = -\nabla p + \boldsymbol{J} \times \boldsymbol{B} + \nabla \cdot \mu \rho \nabla \boldsymbol{V}, \qquad (2)$$

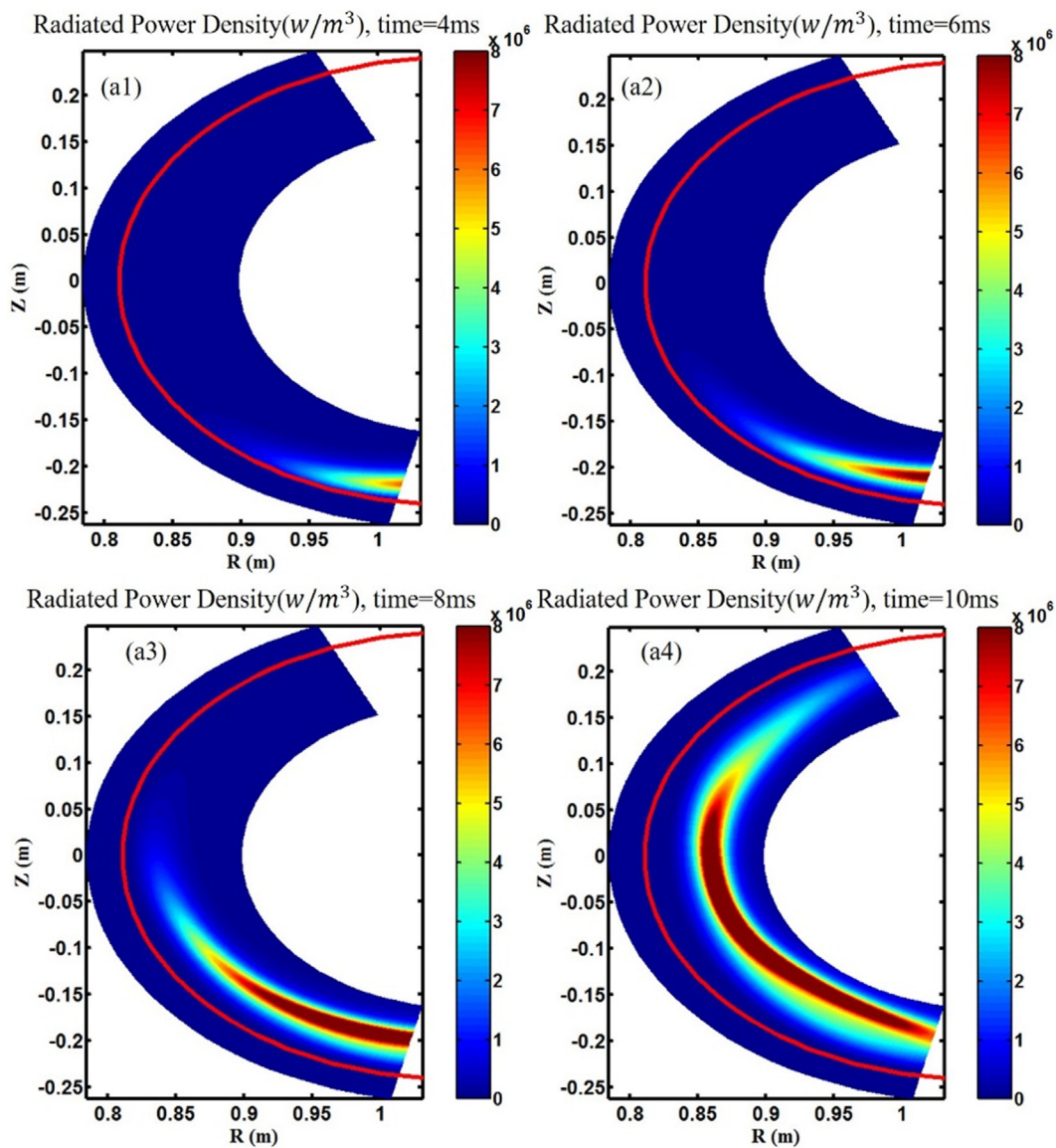**FIG. 6.** Poloidal distribution of radiation power density at the toroid of 30° HFS edge: (a1) 4; (a2) 6; (a3) 8; and (a4) 10 ms.

$$\frac{\partial \boldsymbol{B}}{\partial t} = \nabla \times (\boldsymbol{V} \times \boldsymbol{B}) - \nabla \times \eta \boldsymbol{J}, \tag{3}$$

$$n_e \frac{\partial T_e}{\partial t} = (\gamma - 1)[n_e T_e \nabla \cdot \boldsymbol{V} + \nabla \cdot \boldsymbol{q}_e - Q_{loss}], \tag{4}$$

$$q = -n\left[\chi_{\|}\mathbf{bb} + \chi_{\perp}(1 - \mathbf{bb})\right] \cdot \nabla T, \tag{5}$$

$$\frac{dn_e}{dt} + n_e \nabla \cdot \boldsymbol{V} = \nabla \cdot D \nabla n_e + S_{ion/rec}, \tag{6}$$

$$\frac{dn_i}{dt} + n_i \nabla \cdot \boldsymbol{V} = \nabla \cdot D \nabla n_i + S_{ion/3\text{-}body}, \tag{7}$$

$$\frac{dn_z}{dt} + n_z \nabla \cdot \boldsymbol{V} = \nabla \cdot D \nabla n_z + S_{ion/rec}. \tag{8}$$

Equation (2) is the momentum equation; Eq. (3) gives Maxwell's equations coupled with Ohm's law, where ρ is the plasma mass density, $\boldsymbol{v}$ denotes velocity, p is the pressure, and $\boldsymbol{J}$ represents the current density; and Eq. (4) represents the single-fluid temperature equation, where $\boldsymbol{q}_e$ is the heat flux and Q_{loss} is the source/sink term.

In the NIMROD model, it was assumed that the ion temperature was equal to the electron temperature. Moreover, the heat flux $\boldsymbol{q}_e$ was calculated by Eq. (5) and parameterized by the temperature-dependent anisotropic thermal conductivities, $\chi_{\|} \propto T^{\frac{5}{2}}$ and $\chi_{\perp} \propto T^{-1/2}$. The value of Q_{loss} was obtained by the KPRAD module, which calculated ionization, radiation, and recombination of the impurity species; also, Ohmic heating was included in this term. The KPRAD module traced the ionized impurities along with the main plasma ions, as shown in Eqs. (6)–(8). These equations express the source and sink terms included in the evolution equations of the NIMROD code for density. The source/sink term included contributions from the ionization, recombination, and three-body recombination of impurities.

The initial equilibrium used in the simulation was obtained by the reconstruction with the equilibrium fitting code (EFIT), which was based on the J-TEXT shot No. 1 075 464. The experimental results are given in Sec. II. The wall and limiter of the J-TEXT tokamak were composed of graphite, so impurities were mainly from carbon. The main input parameters of the density limit density simulation are given in Table I. In order to make the S value (the Lundquist number) close to the experiment, the resistivity of this paper was set to be smaller than that of J-TEXT. A series of J-TEXT simulations were run with the resistivity $\eta = 4.9 \times 10^{-8}\,\Omega\,m$. The parameter of the Lundquist number is calculated in the NIMROD code, and the value is approximately 9.5×10^6, which is similar to the value of general J-TEXT experiments (about 1×10^7). A series of the J-TEXT simulations were performed with the resistivity of $\eta = 4.9 \times 10^{-8}$. The perpendicular thermal diffusion in the simulation was defined by the initial values of $\chi_{\perp}$ of 0.1 m^2/s in the core and 1 m^2/s at the edge, and the parallel thermal diffusion was defined by the initial values of $\chi_{\|}$ of 1×10^8 m^2/s in the core and 1×10^5 m^2/s at the edge. The values of the thermal diffusion were of the same order as the experimentally obtained values during the normal J-TEXT discharge operation. The particle diffusion coefficient was 1 m^2/s. The other parameter settings are shown in Table I. They were in accordance with the experimental measurement results of the J-TEXT. In addition, to realize the phenomenon of thermal instability, impurities were introduced at the lower window near the inner wall by the KPRAD module of the NIMROD code. The contour of the poloidal distribution of carbon impurities introduced at the initial time is presented in Fig. 4, which

corresponds to the position of the lower limiter in the J-TEXT; the blue circle represents the vacuum and plasma regions.

IV. SIMULATION RESULTS

A. Toroidal symmetric structure of thermal radiation

The toroidal distribution of radiation power density expressed in different contours of toroid angle from 30° to 360° is presented in Fig. 5, where each contour represents a poloidal distribution of radiation, and the black line connects the position of maximum radiation in each poloidal plane. Although impurities were introduced from the position of the lower window limiter, the results showed a toroidal symmetric, a poloidal asymmetric radiative structure that appeared at the high-field side boundary, so the simulation reproduced the experimental characteristics of the MARFE. The poloidal distributions of the radiation power density at the toroid of 30° in Fig. 5 at different times are presented in Fig. 6. From 4 to 10 ms, the local radiation region increased, moving from the lower regions of the last closed magnetic surface (LCFS) to the HFS, and then entered the inner plasma regions.

B. Thermal instability evolution

The thermal instability of the plasma edge is greatly related to the characteristics of carbon radiation. The dependence between the cooling rate of carbon impurities and temperature is shown in Fig. 7. As shown in Fig. 7, there was a nonlinear radiation interval of carbon impurities wrapped in the dark orange region, with temperatures ranging from 10 to 35 eV. When the plasma temperature dropped into the dark orange region, the reduction in temperature caused a nonlinear increase in radiation. Under the J-TEXT high-density discharges, the boundary temperature measured by the probe at the initial time was approximately 50 eV, which more easily entered the nonlinear radiation range of carbon impurities and triggered thermal instability.
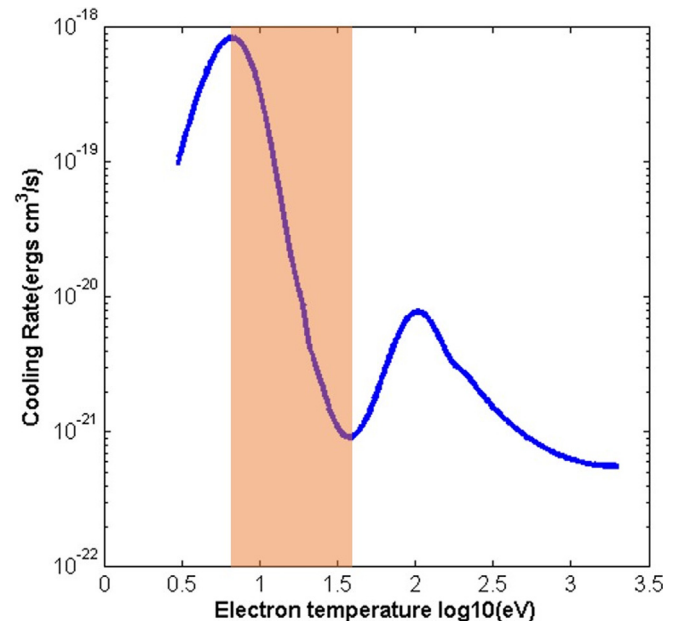

FIG. 7. Cooling rate of carbon impurities as a function of temperature.

To examine the evolution of plasma temperature, density, and radiation at the HFS boundary, it was necessary to analyze thermal instability further. The temporal evolutions of temperature, radiation power density, and plasma density at different radial positions on the HFS boundary are presented in Fig. 8, where the dark orange region corresponds to the upper and lower limiters of the nonlinear radiation interval of carbon impurities (i.e., the dark orange region in Fig. 7). As shown in Fig. 8(a), when the temperature decreased to 35 eV, the

radiation increased rapidly, so the local temperature reduced faster. When the temperature decreased to approximately 10 eV and exited the nonlinear interval, the radiation began to decrease. In Fig. 8(a), the blue arrow indicates that the radiation growth was a slow inward propagation process along the radial direction. The dark orange region increased and moved inward, corresponding to the contours of radiation at different time points in Fig. 6. Furthermore, as shown in Fig. 8(b), the growth rate of plasma density increased during the nonlinear radiation interval
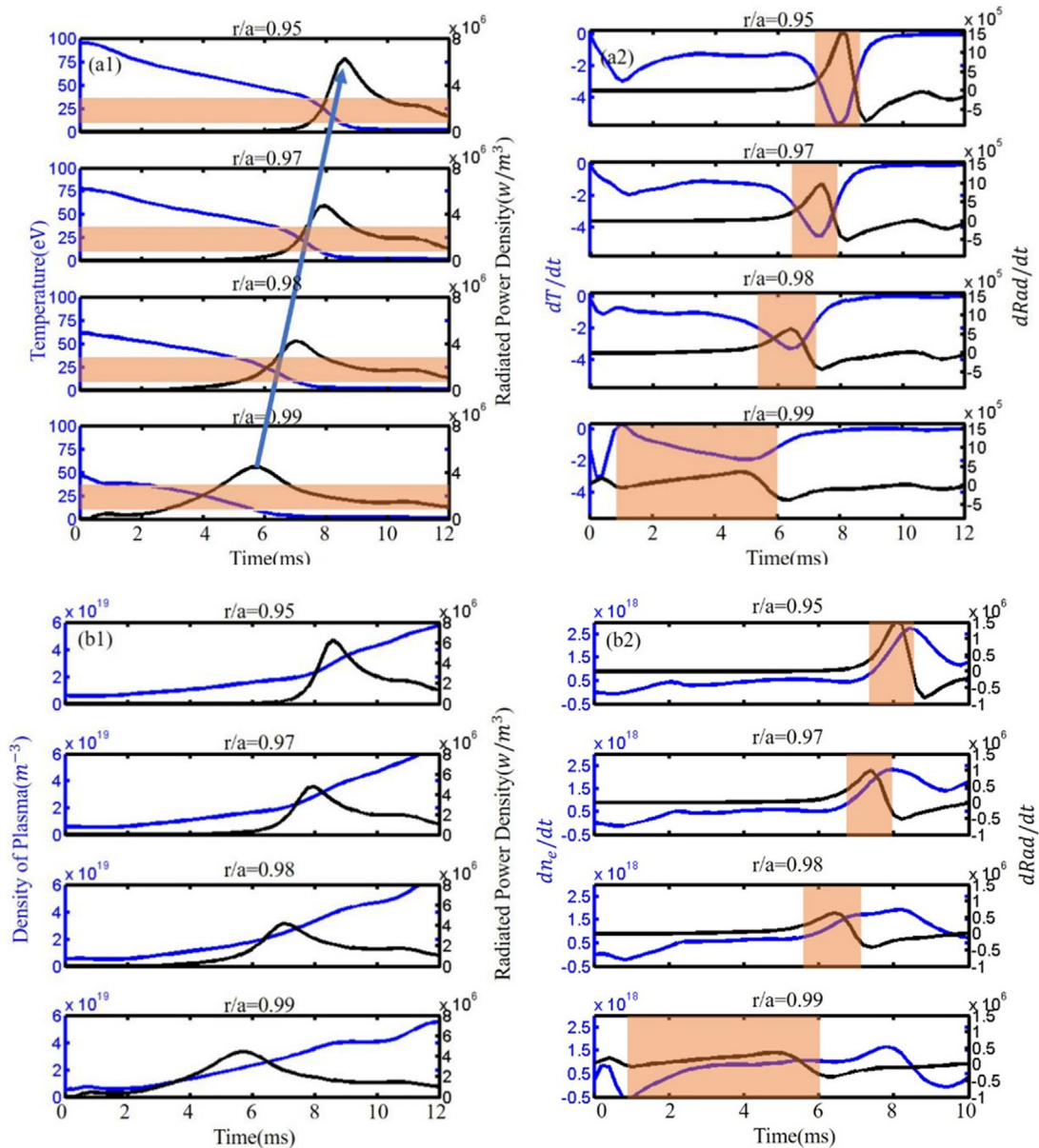
FIG. 8. (a1) Temporal evolution of temperature and radiated power density at different radial positions on the HFS boundary. The blue and black lines represent temperature and radiated power density, respectively: (a2) The derivative of the curves in (a1), where red areas indicate the duration of the nonlinear radiation range. (b1) Temporal evolution of plasma density and radiated power density at different radial positions on the HFS boundary. The blue and black lines represent plasma density and radiated power density, respectively. (b2) The derivative of the curves in (b1), where red areas denote the duration of the nonlinear radiation range.

of carbon impurities. Although the plasma density was continuously increasing, during the nonlinear interval, the growth rate of plasma density was higher than that in the nonlinear region. Consequently, the results in Fig. 8 indicate that thermal instability appeared during the nonlinear radiation interval of carbon impurities.

C. Effects of thermal instability on plasma density limit disruption

After the appearance of thermal instability, the local radiation was enhanced, and the temperature decreased rapidly. The radial profiles of temperature at different times are presented in Fig. 9(a), where the red line corresponds to the initial radial positions of $q = 2$; the temperature decrease at the boundary position can be observed clearly. The contour plots of the temperature alteration ratio after the appearance of thermal instability are shown in Fig. 9(b), where it can be seen that the boundary temperature changed more significantly. As shown in Figs. 9(b1) and 9(b2), the temperature alteration ratio gradually

increased with the expansion of the thermal instability region and the enhancement of radiation.

The enhancement of the thermal instability had a deep influence on the plasma profiles, resulting in a rapid decrease in the boundary plasma temperature, shrinking the local current channel. The current density contours on the high-field side at different times are presented in Fig. 10(a). As shown in Figs. 10(a1) and 10(a2), the current density channel shrank near the LCFS. The shrinkage of the current density increased the radial gradient profiles of the current density, as shown in Fig. 11, where the temporal evolution of the plasma current density gradient at different radial positions near the $q = 2$ surface is presented. The current density gradient increased gradually from outside to inside the $q = 2$ surface.

The increase in the current density gradient triggered the MHD tearing mode. The temporal evolution of amplitude ($\delta B / B \approx \sqrt{W_{mag,n} / W_{mag,0}}$) in n toroidal modes is shown in Fig. 12(b), where the blue line that represents the magnetic perturbation at $n = 1$ gradually expanded after 8 ms. After 13 ms, the amplitude of the higher-order n toroidal modes also increased, as indicated by green and red lines in
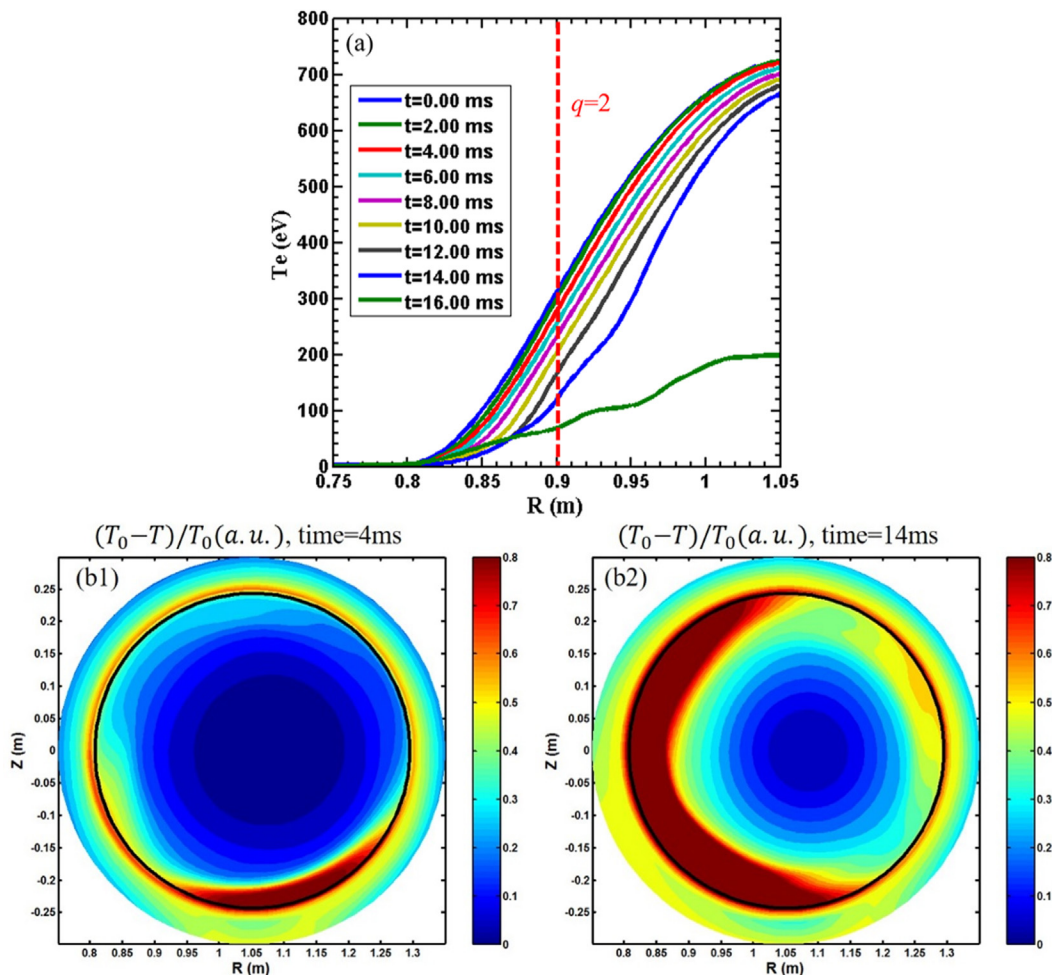
FIG. 9. (a) Radial profiles of temperature at different time slices. (b) Contours of temperature alteration ratio $[(T_0 - T)/T_0(a.u.)]$, where T_0 is the initial equilibrium temperature, and T is the plasma temperature at different times: (b1) 4 and (b2) 10 ms. The black circle denotes the LCFS.
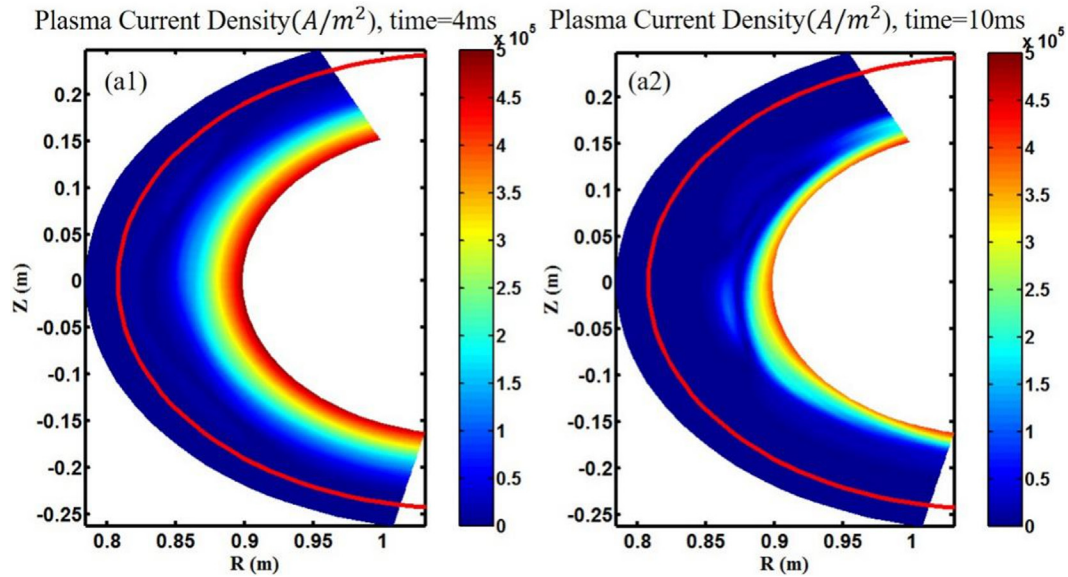
FIG. 10. Poloidal distribution of plasma current density; the blue sector represents vacuum and plasma regions at the HFS edge: (a1) 4 and (a2) 10 ms.

Fig. 12(b), demonstrating the rapid growth of the MHD instabilities after the thermal instability decreased and the current channel constricted.

The Poincaré plots at different times are presented in Figs. 13(a)–13(f), where it can be seen that after 8 ms, the 2/1 island enlarged, the growth of the 2/1 island destabilized the 3/1 mode, and the 3/2 mode appeared after 14 ms. The rapid growth of the magnetic island in Fig. 13(e) corresponds to the lines in Fig. 12(b). In $n = 1$
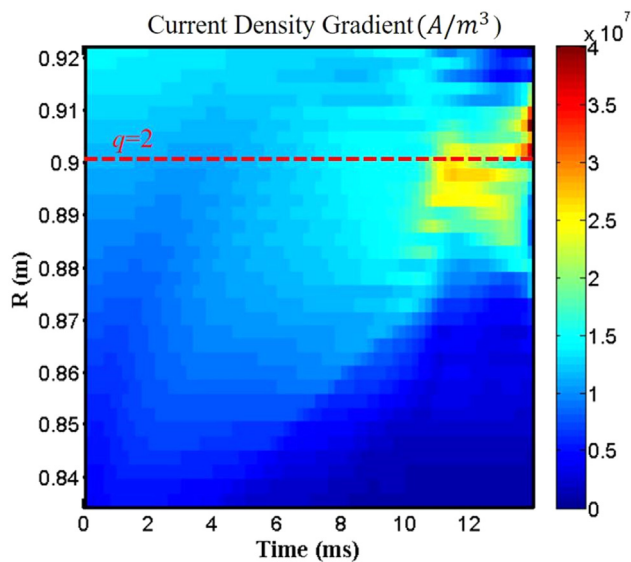

FIG. 11. Temporal evolution of the gradient of the plasma current density at different radial positions.
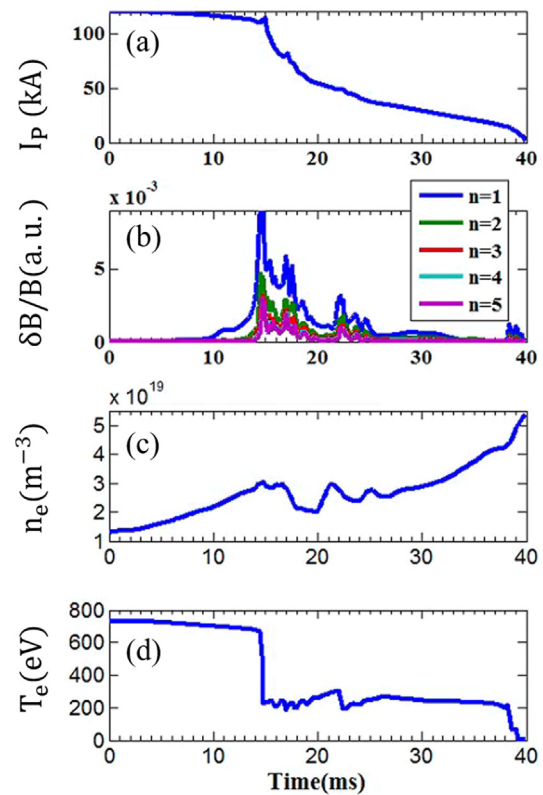

FIG. 12. Temporal evolution of (a) plasma current; (b) amplitude of magnetic perturbation in n toroidal modes; (c) central line-averaged density; and (d) max temperature at core.
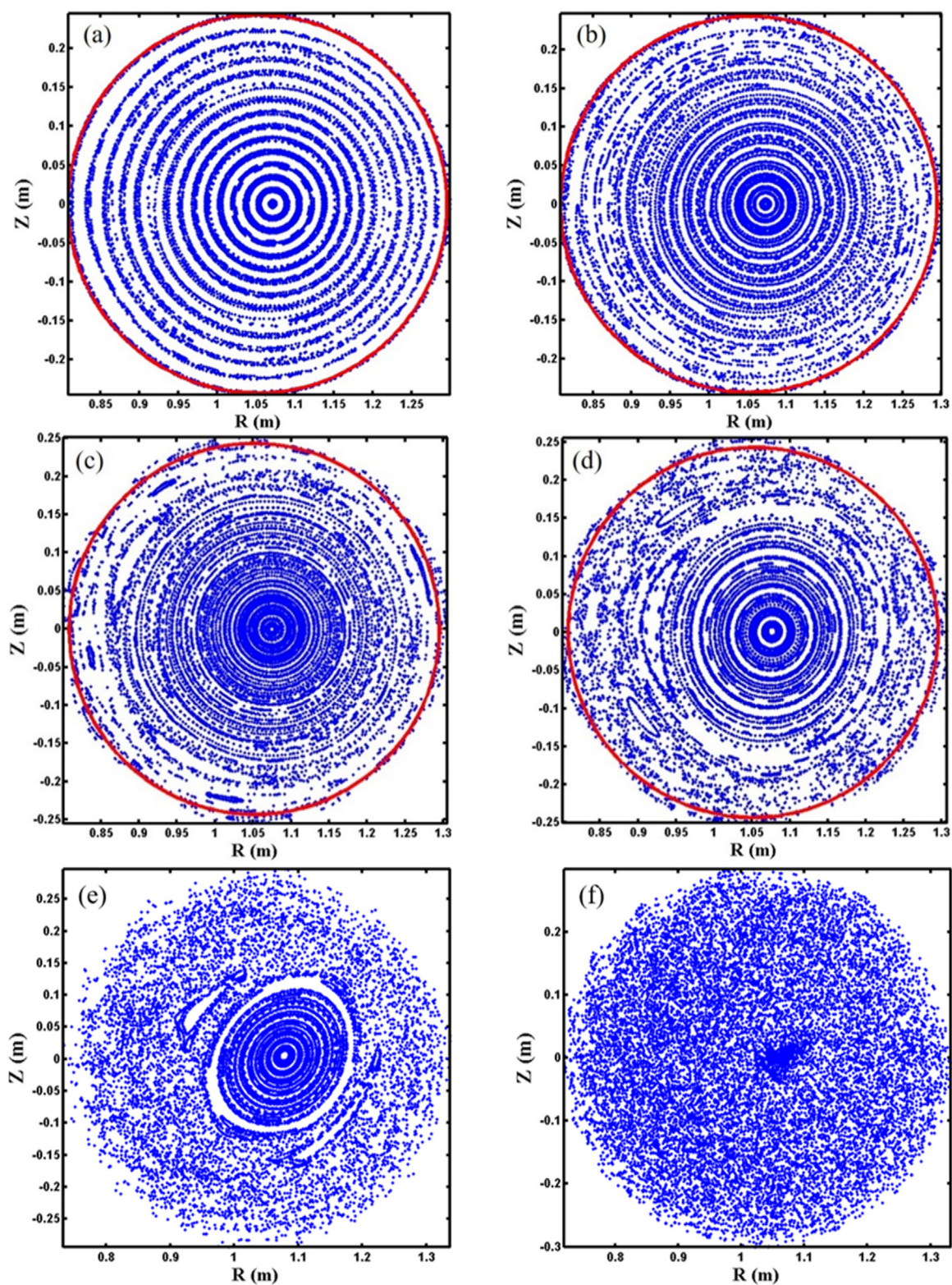
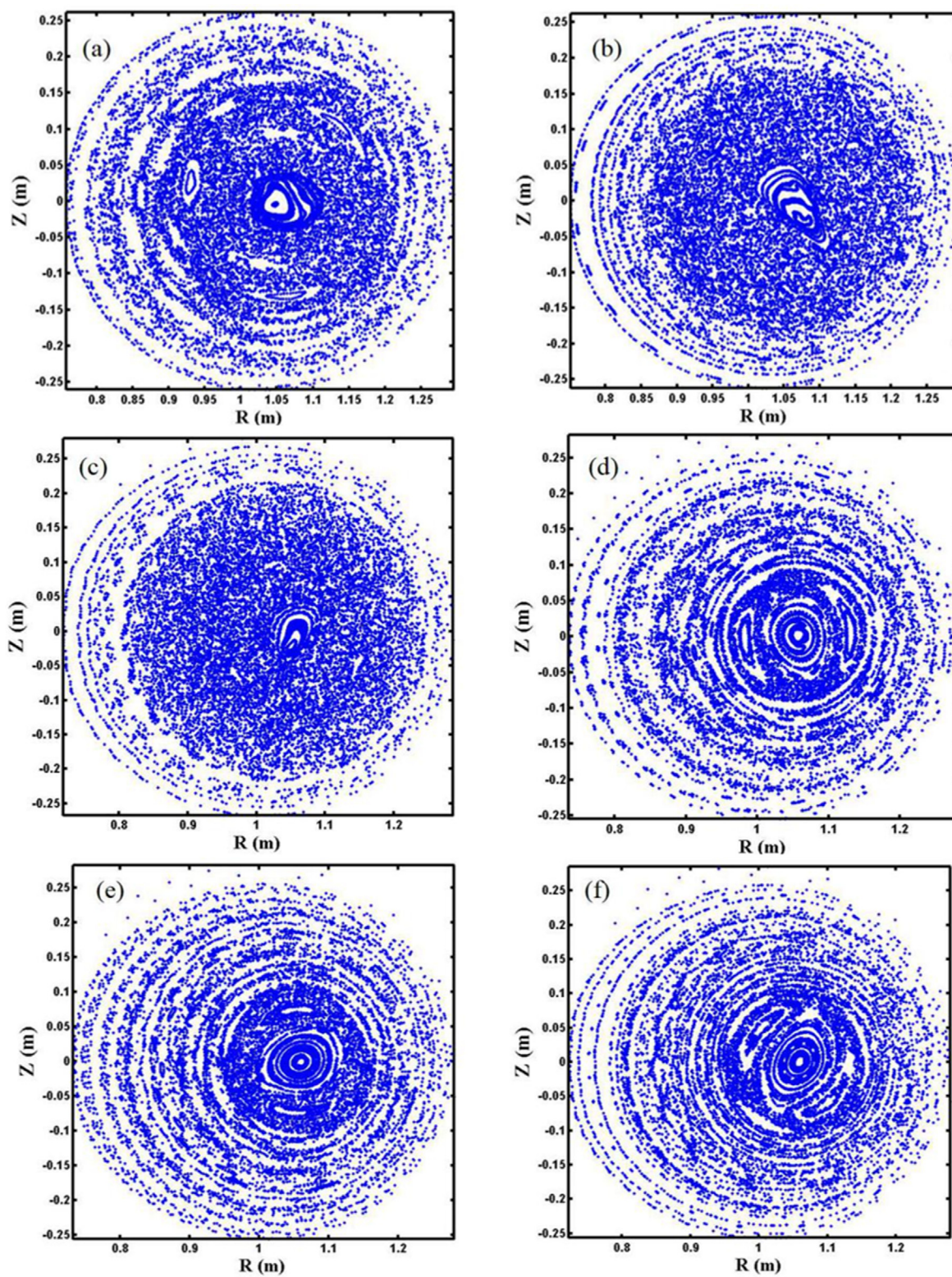**FIG. 13.** Poincaré plots and different times: (a) 6; (b) 8; (c) 10; (d) 12; (e) 14; and (f) 16 ms.

FIG. 14. Poincaré plots and different times: (a) 20; (b) 22; (c) 25; (d) 26; (e) 27; and (f) 28 ms.

mode, the amplitude of magnetic perturbation and its growth rate increased with time. Then, the other higher-order modes stabilized successively. Finally, with the increase in instability, the width of the magnetic island increased, and the magnetic surface was severely stochastic at 15 ms. The plasma confinement was lost, the core temperature began to decrease rapidly, and a thermal quench (TQ) occurred. The evolution process of the maximum core temperature over time is presented in Fig. 12(d). It should be noted that the simulation results of the central line-averaged density in Fig. 12(c) are different from the line-averaged density of the J-TEXT shot No. 1 075 464 in Fig. 1(d). This could be because in the physical model of the NIMROD code, ionization and three-body recombination were included. After 15 ms, thermal quenching occurred, as shown in Fig. 12(d), but the plasma core still maintained a high temperature of approximately 200 eV. Moreover, ionization further increased the plasma density. Therefore, it was necessary to perfect the heat transport mechanism in the physical model of the NIMROD code. In addition, the field line healing occurred, as shown in Fig. 14, and the healing of magnetic field lines also confined the electrons in the plasma core region.

V. DISCUSSION AND SUMMARY

In this paper, the KPRAD module of the NIMROD code is used to study thermal instability when introducing impurities. However, the physical model of the NIMROD code does not include localized hydrogen recycling and plasma–wall interaction mechanisms,[38–42] so the carbon impurity produced from the lower window limiter is artificially injected near the limiter region outside the LCFS. According to the effective Z value of the J-TEXT tokamak, the usual carbon content is less than 5% of the electron number, so this value is used as an upper limit of total carbon impurities in this study. Hydrogen gas is injected through gas puffing in the J-TEXT. Under the above-presented model scheme, thermal instability and MARFE are numerically reproduced, and the density limit disruption is triggered. The full self-consistent simulation of thermal instability can be carried out only after the physical model of hydrogen recycling and plasma–wall interaction is implemented into the related numerical codes. Another difficulty is the lack of reliable measurement tools for the TQ time. However, the authors believe that the simulation TQ time presented in this paper is far from its real value. This can be because most of the density limit disruption on the J-TEXT is related to the locked modes (LMs). Still, the physical model of the NIMROD code may not include the heat transport mechanism induced by locked modes (LMs).[43,44] The collisionless plasma transport of LMs is studied to understand the underlying mechanisms of thermal quenching physics in tokamak disruption.[45] The self-consistent simulation of the heat transport mechanism during the density limit disruption should include the mechanism of LMs and plasma transport in stochastic magnetic fields, but it depends on the development of a theoretical model and numerical codes.

However, this study has certain limitations. Namely, the discharge considered in this study is Ohmic discharge. The numerical simulation of thermal instability and density limit disruption under the electron cyclotron resonance heating (ECRH) could be analyzed in future work. Still, first, it is necessary to determine how the NIMROD code uses the J-TEXT parameter to realize the relevant thermal instability and density limit disruption under the ECRH heating.[46] Therefore, additional experiments and numerical simulations are necessary.

In summary, this study analyzes the evolution of thermal instability in J-TEXT density limit discharge through experiments and simulations. The NIMROD code is used to simulate thermal instability, focusing on the relationship between thermal instability and density limit disruption. The evolution results of thermal instability show that the boundary temperature decreases rapidly after the appearance of thermal instability. Furthermore, the radiation increases rapidly with a decrease in temperature, and the temperature decreases further with the radiation intensity. Considering the relationship between the thermal instability and the density limit disruption, this paper shows that the local cooling of thermal instability at the plasma edge shrinks the local current channel and enhances the internal current density gradient, which triggers the 2/1 mode and destabilizes the 3/1 and other higher-order modes. Eventually, the rapid growth of MHD instability will result in a density limit disruption.

AUTHOR DECLARATIONS
Conflict of Interest

The authors have no conflicts to disclose.

Author Contributions

Jianjun Yuan: Data curation (equal); Methodology (equal); Software (equal); Writing – original draft (equal); Writing – review & editing (equal). **Zhonghe Jiang:** Methodology (lead); Software (equal); Validation (equal); Writing – review & editing (lead). **Yunfeng Liang:** Methodology (lead); Validation (equal). **ZiXiao Jiao:** Data curation (equal); Software (supporting); Writing – review & editing (supporting). **Zhen Li:** Data curation (supporting); Methodology (supporting). **Jiankun Hua:** Data curation (supporting). **Li Gao:** Writing – review & editing (supporting). **Zhongyong Chen:** Methodology (supporting). **Yonghua Ding:** Supervision (supporting).

DATA AVAILABILITY

The data that support the findings of this study are available within the article.

REFERENCES

[1]M. Murakami, J. D. Callen, and L. A. Berry, "Some observations on maximum densities in tokamak experiments," Nucl. Fusion **16**(2), 347–348 (1976).
[2]S. J. Fielding, J. Hugill, G. M. Mccracken, J. W. M. Paul, R. Prentice, and P. E. Stott, "High-density discharges with gettered torus walls in DITE," Nucl. Fusion **17**(6), 1382–1385 (1977).
[3]J. Hugill, P. J. Lomas, and A. J. Wootton, "High density operation in DITE with neutral beam injection," Technical Report No. CLM-R-239 (1983).
[4]M. Greenwald, J. L. Terry, S. M. Wolfe, S. Ejima, M. G. Bell, S. M. Kaye, and G. H. Neilson, "A new look at density limits in tokamaks," Nucl. Fusion **28**, 2199 (1988).

[5]M. Greenwald, "Density limits in toroidal plasmas," Plasma Phys. Controlled Fusion 44(8), R27–R53 (2002).

[6]J. A. Wesson, R. D. Gill, M. Hugon, and A. Weller, "Disruptions in JET," Nucl. Fusion 29(4), 641–666 (1989).

[7]A. Gibson, "Radiation limits to tokamak operation," Nucl. Fusion 16(3), 546–550 (1976).

[8]D. E. Roberts, "Density and confinement time limits of Ohmically heated tokamaks," Nucl. Fusion 23(3), 311–329 (1983).

[9]D. A. Gates and L. Delgado-Aparicio, "Origin of tokamak density limit scalings," Phys. Rev. Lett. 108(16), 165004 (2012).

[10]D. A. Gates, D. P. Brennan, L. Delgado-Aparicio, Q. Teng, and R. B. White, "Thermo-resistive disruptions and the tokamak density limit," Phys. Plasmas 23(5), 056113 (2016).

[11]Q. Teng, N. Ferraro, D. A. Gates, and R. B. White, "Nonlinear simulations of thermo-resistive tearing mode formalism of the density limit," Nucl. Fusion 58(10), 106024 (2018).

[12]Q. M. Hu, N. C. Wang, Q. Yu, Y. H. Ding, B. Rao, Z. P. Chen, and H. Jin, "Research on the effect of resonant magnetic perturbations on disruption limit in J-TEXT tokamak," Plasma Phys. Controlled Fusion 58(2), 025001 (2015).

[13]M. X. Huang, Q. M. Hu, P. Shi, X. L. Zhang, and G. Zhuang, "The operation region and MHD modes on the J-TEXT tokamak," Plasma Phys. Controlled Fusion 58(12), 125002 (2016).

[14]P. Shi, G. Zhuang, K. Gentle, Q. M. Hu, J. Chen, Q. Li, Y. Liu, L. Gao, X. L. Zhang, and H. Liu, "First time observation of local current shrinkage during the MARFE behavior on the J-TEXT tokamak," Nucl. Fusion 57(11), 116052 (2017).

[15]B. Lipschultz, B. Labombard, E. S. Marmar, M. M. Pickrell, J. L. Terry, R. Watterson, and S. M. Wolfe, "MARFE: An edge plasma phenomenon," Nucl. Fusion 24(8), 977–988 (1984).

[16]B. Lipschultz, "Review of MARFE phenomena in tokamaks," J. Nucl. Mater. 145, 15–25 (1987).

[17]F. P. Boody, C. E. Bush, S. S. Medley, H. K. Park, and J. F. Schivell, "Phenomenology of MARFEs in TFTR," J. Nucl. Mater. 145–147, 196–200 (1987).

[18]V. Mertens, W. Junker, M. Laux, M. Schittenhelm, K. Buchl, F. Mast, A. Carlsont, A. Field, C. Fuchs, and O. Gehre, "Experimental investigation of MARFEs and the density limit in the ASDEX upgrade," Plasma Phys. Controlled Fusion 36(8), 1307 (1994).

[19]X. Gao, Y. P. Zhao, J. R. Luo, Y. X. Jie, and Y. X. Wan, "Improved confinement mode induced by the MARFE on the HT-7 superconducting tokamak," Plasma Phys. Controlled Fusion 41(11), 1349 (1999).

[20]X. Gao, J. R. Luo, Y. P. Zhao, N. Qiu, and Y. X. Wan, "MARFE phenomena in the HT-7 tokamak," J. Nucl. Mater. 279(2–3), 330–334 (2000).

[21]F. A. Kelly, W. M. Stacey, J. Rapp, and M. Brix, "Thermal instability theory analysis of multifaceted asymmetric radiation from the edge (MARFE) in Tokamak Experiment for Technology Oriented Research (TEXTOR)," Phys. Plasmas 8(7), 3382–3390 (2001).

[22]Y. Liang, H. R. Koslowski, F. A. Kelly, M. Z. Tokar, X. Loozen, G. Bertschinger, W. Biel, K. H. Finken, M. W. Jakubowski, and A. Kramer-Flecken, "Influence of the dynamic ergodic divertor on the density limit in TEXTOR," Phys. Rev. Lett. 94(10), 105003 (2005).

[23]D. Dobrott, R. L. Miller, and J. M. Rawls, "Time evolution of thermal instabilities," Phys. Fluids 20(10), 1744 (1977).

[24]A. D. Ploey, M. Goossens, and R. A. M. Van-Der-Linden, "Multifaceted asymmetric radiation from the edge (MARFE's): A general magnetohydrodynamic study in a one-dimensional tokamak model," Phys. Plasmas 1(8), 2623–2629 (1994).

[25]J. Neuhauser, W. Schneider, and R. Wunderlich, "Thermal instabilities and poloidal asymmetries in the tokamak edge plasma," Nucl. Fusion 26(12), 1679–1692 (1986).

[26]J. F. Drake, "Radiative condensation in tokamak edge plasma," Phys. Fluids 30(8), 2429–2433 (1987).

[27]R. B. White, D. A. Gates, and D. P. Brennan, "Thermal island destabilization and the Greenwald limit," Phys. Plasmas 22(2), 022514 (2015).

[28]W. M. Stacey, "A survey of thermal instabilities in tokamak plasmas: Theory, comparison with experiment, and predictions for future devices," Fusion Sci. Technol. 52(1), 29–67 (2007).

[29]A. D. Ploey, R. A. M. Van-Der-Linden, G. T. A. Huysmans, M. Goossens, W. Kerner, and J. P. Goedbloed, "MARFEs: A magnetohydrodynamic stability study of two-dimensional tokamak equilibria," Plasma Phys. Controlled Fusion 39(3), 423–438 (1997).

[30]V. Izzo, "Impurity mixing and radiation asymmetry in massive gas injection simulations of DIII-D," Phys. Plasmas 20(5), 056107 (2013).

[31]V. A. Izzo, P. B. Parks, N. W. Eidietis, D. Shiraki, E. M. Hollmann, N. Commaux, R. S. Granetz, D. A. Humphreys, C. J. Lasnier, R. A. Moyer et al., "The role of MHD in 3D aspects of massive gas injection," Nucl. Fusion 55(7), 073032 (2015).

[32]V. A. Izzo, "The effect of pre-existing islands on disruption mitigation in MHD simulations of DIII-D," Phys. Plasmas 24, 056102 (2017).

[33]Z. H. Jiang, J. Huang, R. H. Tong, T. T. Yang, Z. F. Lin, V. A. Izzo, C. H. Li, Y. F. Liang, X. Ye, Y. H. Ding et al., "Simulations of the effects of pre-seeded magnetic islands on the generation of runaway current during disruption on J-TEXT," Phys. Plasmas 26(6), 062508 (2019).

[34]C. C. Kim, Y. Q. Liu, P. B. Parks, L. L. Lao, and A. Loarte, "Shattered pellet injection simulations with NIMROD," Phys. Plasmas 26(4), 042510 (2019).

[35]V. A. Izzo, "Interpretive MHD modeling of dispersive shell pellet injection for rapid shutdown in tokamaks," Nucl. Fusion 60(6), 066023 (2020).

[36]Z. H. Jiang, T. T. Yang, J. J. Yuan, C. H. Li, Y. Liang, J. Huang, and Z. Y. Chen, "Minor disruptions triggered by supersonic molecular beam injection on the J-TEXT tokamak," Nucl. Fusion 60(6), 066004 (2020).

[37]C. H. Li, Z. H. Jiang, Z. F. Lin, X. Ye, J. Huang, R. H. Tong, L. Z. Zhu, Z. Y. Chen, Y. Liang, P. Zhu et al., "The effect of 2/1 pre-existing magnetic islands width on the suppression of runaway electrons in disruption simulations of J-TEXT," Plasma Phys. Controlled Fusion 62(9), 095010 (2020).

[38]W. M. Stacey and T. W. Petrie, "The role of thermal instabilities in limiting the density in DIII-D," Phys. Plasmas 7(12), 4931–4941 (2000).

[39]M. Z. Tokar, "The possible nature of the localized recycling effect on the plasma edge in tokamaks," Plasma Phys. Controlled Fusion 35(9), 1119 (1993).

[40]M. Z. Tokar, J. Rapp, D. Reiser, U. Samm, and P. C. De-Vries, "Localized recycling as a trigger of MARFE," J. Nucl. Mater. 266–269(2), 958–962 (1999).

[41]M. Z. Tokar and F. A. Kelly, "The role of plasma-wall interactions in thermal instabilities at the tokamak edge," Phys. Plasmas 10(11), 4378–4386 (2003).

[42]F. A. Kelly and M. Z. Tokar, "Theoretical study of the effect of the dynamic ergodic divertor on MARFE onset," Contrib. Plasma Phys. 44, 176 (2004).

[43]R. Sweeney, W. Choi, M. Austin, M. Brookman, V. Izzo, M. Knolker, R. J. La Haye, A. Leonard, E. Strait, and F. A. Volpe, "Relationship between locked modes and thermal quenches in DIII-D," Nucl. Fusion 58(5), 056022 (2018).

[44]Q. Hu, X. Du, Q. Yu, N. C. Logan, E. Kolemen, R. Nazikian, and Z. H. Jiang, "Fast and pervasive heat transport induced by multiple locked modes in DIII-D," Nucl. Fusion 59(1), 016005 (2019).

[45]M. G. Yoo, W. X. Wang, E. Startsev, C. H. Ma, S. Ethier, J. Chen, and X. Z. Tang, "Collisionless plasma transport mechanisms in stochastic open magnetic field lines in tokamaks," Nucl. Fusion 61(12), 126036 (2021).

[46]T. G. Jenkins and E. D. Held, "Coupling extended magnetohydrodynamic fluid codes with radiofrequency ray tracing codes for fusion modeling," J. Comput. Phys. 297, 427 (2015).